NANO LETTERS
Letter
Cite This: Nano Lett. 2019, 19, 100−107
pubs.acs.org/NanoLett

Toward High-Contrast Atomic Force Microscopy-Tip-Enhanced Raman Spectroscopy Imaging: Nanoantenna-Mediated Remote-Excitation on Sharp-Tip Silver Nanowire Probes

Xuezhi Ma,[†] Yangzhi Zhu,[‡] Ning Yu,[‡] Sanggon Kim,[‡] Qiushi Liu,[†] Leonard Apontti,[‡] Da Xu,[†] Ruoxue Yan,[‡,§] and Ming Liu*[,†,§]

[†]Department of Electrical and Computer Engineering, [‡]Department of Chemical and Environmental Engineering, and [§]Material Science and Engineering program, University of California, Riverside, California 92521, United States

Supporting Information

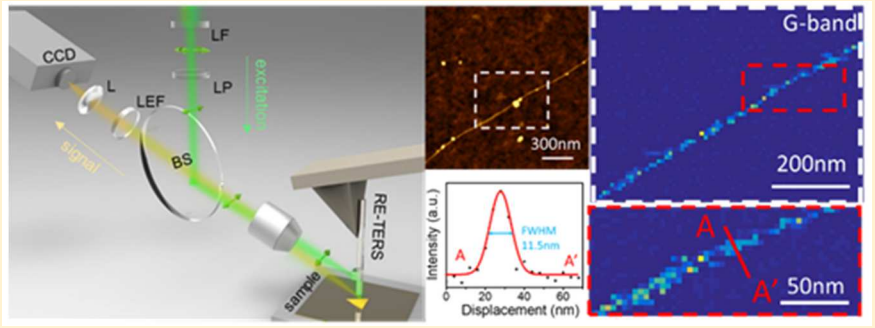

ABSTRACT: The tip-enhanced Raman spectroscopy (TERS) imaging technique is designed to provide correlated morphological and chemical information with a nanoscale spatial resolution by utilizing the plasmonic resonance supported by metallic nanostructures at the tip apex of a scanning probe. However, limited by the scattering cross sections of these nanostructures, only a small fraction of the incident light can be coupled to the plasmonic resonance to generate Raman signals. The uncoupled light then directly excites background spectra with a diffraction-limited resolution, which becomes the background noise that often blurs the TERS image. Here, we demonstrate how this problem can be solved by physically separating the light excitation region from the Raman signal generation region on the scanning probe. The remote-excitation TERS (RE-TERS) probe, which can be fabricated with a facile, robust and reproducible method, utilizes silver nanoparticles as nanoantennas to mediate the coupling of free-space excitation light to propagating surface plasmon polaritons (SPPs) in a sharp-tip silver nanowire to excite Raman signals remotely. With this RE-TERS probe, a 10 nm spatial resolution was demonstrated on a single-walled carbon nanotube sample, and the strain distribution in a monolayer molybdenum disulfide (MoS_2) was mapped.

KEYWORDS: *Tip-enhanced Raman spectroscopy imaging, remote-excitation, plasmonic antenna, self-assembly, stress-mapping, high spatial resolution*

Scanning probe microscopies (SPM), such as scanning tunneling microscopy (STM) and atomic force microscopy (AFM), have become powerful tools for acquiring morphology information on nanostructured surfaces with atomic resolutions but offer limited insights into their surface chemistry. On the other hand, far-field optical spectroscopies, such as Raman or Fourier-transform infrared spectroscopy (FTIR), are widely used to investigate chemical bonds and molecular interactions. Their spatial resolutions, however, are orders of magnitude lower, dictated by the diffraction limit of the excitation light. Combining these two technologies has led to the development of tip-enhanced Raman/FTIR spectroscopy (TERS and nano-FTIR) imaging techniques,[1−8] which bear the potential for chemical analysis of complex nanoscale surfaces down to the single molecule resolution.[9] In these applications, the tip apex of a metal probe, typically tens of nanometers in curvature, serves as a plasmonic antenna to amplify the intensity of both the incident light (i.e., excitation) and the Raman-scattered light (i.e., signal) and confines them to a nanoscale mode volume to achieve a spatial resolution defined by the curvature of the tip apex. However, because the excitation efficiencies of plasmonic nanostructures are generally small, only a tiny fraction of the incident power can be concentrated at the tip. The uncoupled light can still excite Raman scattering processes on the sample with low spatial resolution, which not only generates background noises that reduces the signal-to-noise ratio but also increases the

Received: August 22, 2018
Revised: November 2, 2018
Published: December 4, 2018

DOI: 10.1021/acs.nanolett.8b03399
Nano Lett. 2019, 19, 100−107

chance of sample photodegradation, giving the fact that strong lasers are often used to pump the TERS signal. To tackle these problems, grating-assisted plasmonic-nanofocusing probes have recently emerged as a promising solution for low-background-noise TERS acquisition.[10−12] In these designs, the incident light is converted to SPPs through grating couplers that are fabricated on the probe sidewall with a few microns away from the probe apex. Depending on the coupler design, coupling efficiencies have been achieved between 0.1−9%. The excited SPPs propagate toward the probe apex along the tapered probe and become further compressed by the conical geometries for high-spatial-resolution near-field imaging. Because the SPP excitation region is separated from the Raman acquisition region, the Raman noise from the uncoupled incident light is drastically reduced.

Compared with other TERS techniques, grating-assisted nanofocusing skips the noise reduction steps, such as the background subtraction method or the modulation method,[13] and has been used in a broad spectrum of research topics, ranging from optical nanoimaging,[14] Raman analysis,[11] to nanoscale ultrafast optics.[15] However, the reproducibility of the grating-assisted probes has been the primary challenge to this technique. For example, annealed gold wires, which are the preferred material for fabricating grating-assisted probes due to their high crystallinity and low plasmonic loss, suffer from the low mechanical stiffness as a result of the annealing.[16] The intricate balance between the mechanical stiffness and optical quality of the gold wires requires meticulous control over annealing conditions. Equally tricky is the precise control over the electrochemical etching process used to taper the nanowire (NW) tip, the exact geometry and surface roughness of which are critical for the efficiency of plasmonic nanofocusing and TERS enhancement.[17]

Compared with gold, silver is more favorable for TERS experiments due to its stronger plasmonic enhancement and lower fluorescence background. Chemically synthesized crystalline silver nanowires (AgNWs), in particular, are uniquely suited for TERS due to their nanoscale field confinement,[18,19] mechanical robustness, and low plasmonic loss,[20,21] the latter of which both stemming from their polytwined crystalline nature. In addition, AgNW SPPs can be excited easily using a variety of methods, such as from prism or grating couplers,[22] near-field coupling,[21,23,24] to as simple as tip, defect, and nanoantenna scattering,[25,26] making them uniquely suited for remote-excitation TERS as an easy alternative to the grating-assisted nanofocusing technique.

Recently, we reported the synthesis of AgNWs that have ultrasharp conical tips with nanometer-scale tip curvature, and their integration with commercial AFM probes for topographical imaging.[20] In the present article, we demonstrate that high-resolution remote-excitation TERS imaging can also be realized with an AFM-mounted sharp-tip AgNW. This RE-TERS probe utilizes colloidal silver nanocubes (AgNCs) attached to the AgNW probe to couple visible light into SPPs on the latter. Benefiting from the low plasmonic loss of the free-standing AgNW at the visible wavelengths,[21] the propagation loss of SPPs along the NW can be maintained at less than 1 dB when the AgNC is placed only a few microns away from the tip apex. The conical taper at the AgNW tip leads to the further compression of the SPP mode and the generation of a plasmonic hot spot at the tip apex to allow high spatial resolution TERS imaging. Adding to the inherent low background noise of the remote-excitation scheme, the AgNC antenna is insensitive to the polarization of the incident light, which allows the use of linearly polarized light with the electric field parallel to the metallic substrate to further reduce the background Raman noise from stray beams. With the AgNC−AgNW RE-TERS probe, we demonstrated the TERS imaging of monolayer molybdenum disulfide (MoS_2) domains and estimated the spatial resolution around 41 nm and TERS contrast around 100. The spatial resolution can be further pushed to ∼10 nm when a single-walled carbon nanotube (SW-CNT) sample is characterized.

Results and Discussion. As illustrated in Figure 1a, the RE-TERS probe was installed on a commercial AFM-TERS system (SmartSPM 1000, AIST-NT) with modifications to enable polarization adjustment of the incident laser. To launch the SPPs into the AFM-mounted AgNW probe, a linearly polarized laser (532 nm, *s*-polarization) was focused on the AgNC attached to the side wall of a NW at an incident angle of ∼25° by a microscope objective (100×) with a numerical aperture (NA) of 0.7 and a long working distance of 6 mm. The excited SPPs propagate along the NW and get further compressed by the conical geometry of the NW tip to generate a nanosized hot spot at the tip apex for TERS excitation. The TERS signal scattered by the AgNW tip is then collected through the same objective lens. To maintain the remote-excitation condition, the NC needs to be at least several micrometers away from the NW tip (Figure 1b), so that the tip sits well outside the laser focus (∼1 μm × 0.9 μm). By raising

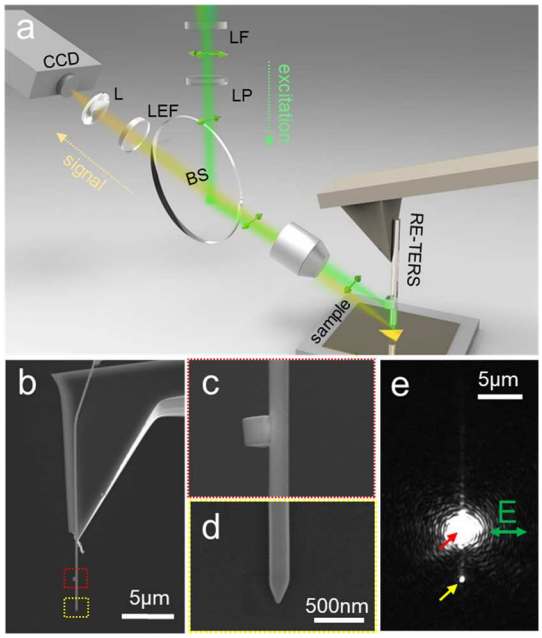

Figure 1. (a) Schematic illustration of the RE-TERS setup. The green excitation laser beam (532 nm) is sent through a laser line filter (LF), a linear polarizer (LP), and a beam splitter (BS) to an objective lens, which focuses it on an AgNC to excite SPPs on the AgNW waveguide. The SPPs propagate toward the tapered tip to excite TERS signals, which are collected through the same objective lens, filtered by a long-pass edge filter (LEF), focused by a lens (L) and collected by a CCD spectrometer. (b) A SEM image of a RE-TERS probe. (c,d) Close-up SEM images of the AgNC−AgNW junction (c) and sharp AgNW tip (d). (e) An image obtained in bright-field optical microscopy showing the coupling between the 532 nm excitation laser beam (polarization along the green arrow) and the AgNC−AgNW junction coupler (red arrow). The yellow arrow marks the position of the AgNW tip.

DOI: 10.1021/acs.nanolett.8b03399
Nano Lett. 2019, 19, 100−107

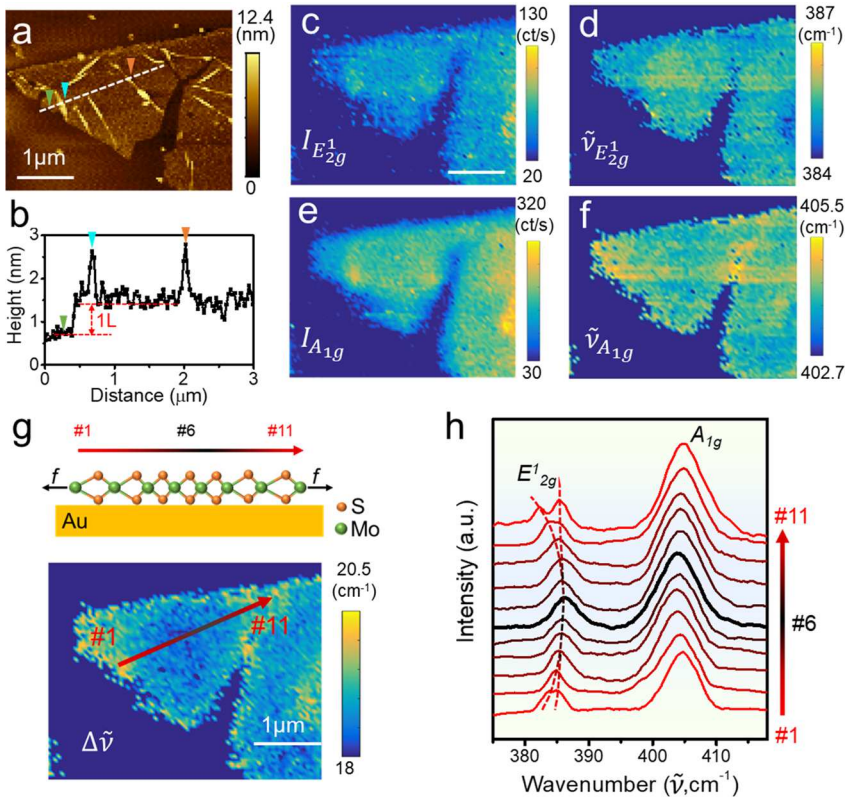

Figure 2. RE-TERS mapping of a CVD-grown MoS_2 monolayer flake. (a) AFM image of the MoS_2 flake on an ultrasmooth gold substrate with the line-scan shown in (b). The markers indicate the edge of the MoS_2 flake (green) and two wrinkles (light blue and orange). (c–f) TERS mapping of the intensities, I (panels c and e, in counts per second, ct/s) and the Raman shifts, $\tilde{\nu}$ (d,f) of the E^1_{2g} and A_{1g} peaks of the MoS_2 flake, respectively. (g,h) Stress-induced Raman peak shifts in MoS_2 monolayer. The bottom panel of (g) shows the interpeak spacing, $\Delta\tilde{\nu}$, between the E^1_{2g} and A_{1g} peaks, which changes from ~18 cm^{-1} at the center to ~20.5 cm^{-1} along the edge of the flake. A series of 11 spectra (h) taken along the red arrow in (g) shows the shifting of both peaks and the splitting of the E^1_{2g} peak toward the edge of the flake (#1 and #11), which is the consequence of the increased tensile stress at the edge as shown in the schematic in the top panel of (g). Excitation: 532 nm, 0.1 mW at sample surface. Integration time = 1 s.

the laser focus away from the sample and choosing the *s*-polarization for excitation, the background noise from direct illumination of the sample is minimized.

AgNCs used here were prepared according to a previously reported polyol synthesis method with slight modification.[27] These AgNCs display high size monodispersity[28] and have an edge length of ~200 nm (Figure 1c). Sharp-tip AgNWs were synthesized following our previously reported method.[20] The crystalline AgNW has smooth surfaces that minimize the propagation loss to ~0.4 dB/μm[21] for the 200 nm in diameter AgNW used in Figure 1b. Given an average of ~3 μm distance between the AgNC and the AgNW tip, the propagation loss of the SPPs was around 1.2 dB. The conical tip tapered to an ultrasharp apex (tip radius ~15 nm, Figure 1d). The AgNC–AgNW bundle was fabricated by incubating a mixture of AgNW and AgNC colloidal solutions for 12 h, during which AgNCs self-assembled on the AgNW surface and the density was adjusted by their relative concentrations (details in Supporting Information). The mixture was then drop-casted on a polydimethylsiloxane (PDMS) substrate, from which a single AgNC–AgNW bundle was picked up with a tungsten tip mounted on a micromanipulator. The excess AgNCs were removed by gently wiping the AgNW with the tungsten tip before picking it up (see SI Video for the demonstration). Then, the AgNC–AgNW bundle with a single AgNC was assembled to the sidewall of the pyramidal tip of a conventional silicon AFM cantilever (Olympus, Model AC160TS-R3), as shown in Figure 1b. This procedure has been demonstrated in our previous report as a simple yet effective fabrication method to prepare high-resolution, high aspect-ratio AFM probes with good stability and performance.[20] The adhesion between a clean AgNW and the silicon tip is sufficient for both AFM tapping mode and contact mode operations. As shown in Figure 1e, when a laser beam is tightly focused on the AgNC (marked by the red arrow), the light coupled out from the AgNW tip 6 μm away from the laser appears clearly as a bright spot (marked by the yellow arrow), demonstrating the successful launching of AgNW SPPs and their propagation to the tip apex. It is worth noting that both the colloidal AgNCs and sharp-tip AgNWs are synthesized in milliliter to liter volumes and the probe fabrication process can be completed under an optical microscope without the need for cost-consuming equipment such as focused ion beam (FIB) etching.

We used the RE-TERS probe to study the strain field on a stressed MoS_2 monolayer flake, for the demonstration of its high-resolution low-background Raman imaging. Raman spectroscopy and microscopy is one of the most powerful tools to study strain and strain distributions in materials,[29] and TERS allows for the visualization of localized strain field with nanoscale resolution.[30−35] Such nanoscale strain characterization capability is extremely important for the micro- and nanoscale strain engineering in MoS_2 and other transition metal dichalcogenides, whose bandgap and optoelectronic

DOI: 10.1021/acs.nanolett.8b03399
Nano Lett. 2019, 19, 100−107

properties can be tuned by applying strains.[36−38] Recently, TERS has been used to probe the strain field of trilayer[39] and monolayer[40] MoS_2 deposited on Au nanocluster arrays, taking advantage of the giant SERS effect from the localized surface plasmon of Au nanoclusters. However, high-resolution TERS strain mapping on a prestressed MoS_2 flake on an ultrasmooth substrate with minimal structural and optical and thermal inhomogeneity has not yet been demonstrated.

In our experiment, the MoS_2 flake was prepared by a standard chemical vapor deposition (CVD) method on a silicon dioxide substrate[41] and transferred onto an ultrasmooth Au thin-film substrate[42] using the capillary-force-assisted clean-stamp transfer technique we recently developed.[43] The flexible PDMS transfer substrate hosting the MoS_2 flake was gently bent before releasing the flake to the Au substrate, to apply a tensile stress on the flake. Figure 2a shows the topographic image of the MoS_2 flake measured with the RE-TERS probe in contact-mode. The stressed MoS_2 flake displayed multiple folds and cracks. The line scan in height (Figure 2b) along the white dashed line demonstrates an ∼0.8 nm film thickness, corresponding well to a MoS_2 monolayer.[44] The root-mean-square (rms) roughness of the Au substrate surface was around 0.32 nm, close to that of a Si wafer.[42] The ultrasmooth Au substrates are important for reducing the contribution of roughness-induced SERS, which could results in artifacts in gap-mode TERS imaging.[45]

Figure 2c−f show the corresponding RE-TERS intensity and Raman shift images of the two major Raman-active modes (E^1_{2g} and A_{1g}) of MoS_2 measured from the same monolayer flake. Near the MoS_2 flake edges, the spectra intensity mapping can be as sharp as one pixel (Figure 2c), indicating that the resolution of the TERS probe is at least as good as the step size (50 nm, details in Supporting Information). In order to quantify the spatial resolution, we did a line-scan across a domain edge and used the error function to fit the intensity data. 41 nm spatial resolution is shown in Figure S4.

In the TERS images, the E^1_{2g} peak at 385.4 ± 0.6 cm^{-1} corresponds to the in-plane vibration of the two S atoms and Mo atom in opposite directions, whereas the A_{1g} peak at 404.1 ± 0.5 cm^{-1} represents the out-of-plane vibration where the two S atoms move in opposite directions perpendicular to the basal plane. The positions of the two Raman peaks are in good agreement with previous reports of monolayer MoS_2[46−49] and are consistent with the layer thickness measured with the topographical mapping. The intensity maps of the two modes (Figure 2c,e) show similar spatial variations that also correspond well with its AFM image: stronger signals were seen where the MoS_2 flake has microscale folds and weaker signal were seen where cracks are found. Such correlations between the MoS_2 morphology and TERS intensity demonstrate the optical uniformity of the ultrasmooth gold substrate. However, the Raman shift maps (Figure 2d,f) of the two modes show completely different trends. The peak position of the E^1_{2g} mode shows consistent red-shifts toward the edges of the flakes and near the cracks, whereas the spatial variation in the A_{1g} mode frequency shows a subtler but opposite pattern. To better visualize the trend, the frequency difference $\Delta\tilde{\nu}$ ($\Delta\tilde{\nu} = \tilde{\nu}_{A_{1g}} - \tilde{\nu}_{E^1_{2g}}$) between the two modes were plotted in Figure 2g. Over the entire flake, $\Delta\tilde{\nu}$ varies from 18.2 to 20.0 cm^{-1} with an average of ∼18.9 cm^{-1}. Although all of this value still fall within the monolayer regime,[46] there is a strong spatial dependence in $\Delta\tilde{\nu}$, which is ∼1.8 cm^{-1} larger at the edges and near the cracks of the flake than at the center. Figure 2h shows a series of 11 TERS spectra collected along the red-arrow pointing from the left edge of the triangular flake to its upper right corner where it was torn due to stress in Figure 2g. Spectrum #6 corresponds to the middle of the arrow and the center of the flake where it appears darkest in Figure 2g with the lowest $\Delta\tilde{\nu}$. Here, the E^1_{2g} and A_{1g} peak positions, line shapes, and their frequency difference show typical MoS_2 monolayer characteristics.[46] However, moving toward both edges of the triangular domain (positions #1 and #11), the doubly degenerated E^1_{2g} peak starts to soften and eventually splits into a higher frequency E^+ mode at ∼384 cm^{-1} and a lower frequency E^- mode that is significantly red-shifted to ∼382 cm^{-1}. According to the strain-dependence studies,[50] the softening and splitting of the E^1_{2g} mode can be attribute to strain-induced symmetry breaking. The reported E^- mode of 4.5 ± 0.3 cm^{-1}/% uniaxial strain placed the largest strain stored at the pinned edge of the stressed MoS_2 flake at ∼0.9%. In comparison, the out-of-plane A_{1g} mode, which is much less sensitive to the uniaxial strain, shows only subtle differences along the red arrow, and the slight blue-shift at the edges may originate from the stronger van der Waals (vdW) interaction between the MoS_2 monolayer and the substrate[51] to sustain the local strain and prevent slipping. Moreover, compared with confocal Raman measurements,[52] the TERS results tend to have a stronger A_{1g} mode, which may originate from the large vertical component of the electric field ($E_\perp$) inside the gap. Detailed discussion can be found in the Supporting Information.

To determine the spatial resolution of RE-TERS in our experimental condition, we acquired high-resolution AFM-TERS images on a single-walled carbon nanotube (SW-CNT) sample, prepared by spraying SW-CNTs solution on an ultrasmooth gold substrate (detailed in Supporting Information) with a step precision of 4 nm as shown in Figure 3. As depicted by a representative spectrum (Figure 3a inset), typical SW-CNT features including scattered D-band, strong G-band, and 2D-band are observed. The spectroscopic images at these bands are illustrated in Figure 3b,d,f, respectively. It is worth noting that the G-band intensity mapping has relatively stable signals along the CNT throughout the scanning. Such signal stability may benefit from the separation of the light coupling region at the AgNC and the Raman excitation region at tip apex, which generates a relatively stable plasmonic hotspot. Meanwhile in a conventional gap-mode TERS, the gap-SPP coupling efficiency at the tip apex is influenced by the optical index of the sample, leading to an unstable TERS signal. As shown in Figure 3c,e, a 10 nm resolution can be achieved on the G-band and D-band, which is close to the instrumental limit.

The coupling efficiency from the far-field excitation to the AgNW SPP modes has strong dependence on the coupling conditions, including the size of the AgNC and the wavelength, polarization, and coupling angle of the incident laser.[53] Finite element analysis (FEA) simulations using a commercial software (COMSOL Multiphysics) were implemented to study the influence of the aforementioned effects to optimize the coupling efficiency, which is defined as the ratio between the electromagnetic energy flux propagating along the AgNW and the power of incident beam. Figure 4a illustrates the parameters used in the simulation. The incident angle (θ) of 65° with respect to the AgNW is predefined by the equipment, and therefore kept constant in the simulation. The azimuth angle ϕ is defined as the angle between the normal direction of

DOI: 10.1021/acs.nanolett.8b03399
Nano Lett. 2019, 19, 100−107

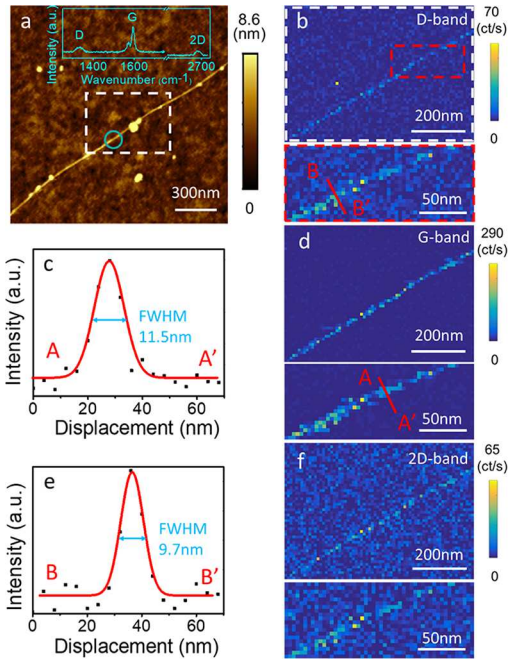

Figure 3. RE-TERS mapping of single-walled CNTs, sprayed on an ultrasmooth Au substrate. (a) AFM morphology imaging. (b) D-band, (d) G-band, and (f) 2D-band intensity images. Spatial steps are 10 nm for top images and 4 nm for the zoom-in at bottom; (c,e) are line cross-section of the marked regions in (d,b). For all TERS mapping, excitation, 532 nm, 0.1 mW at sample surface. Integration time = 1 s.

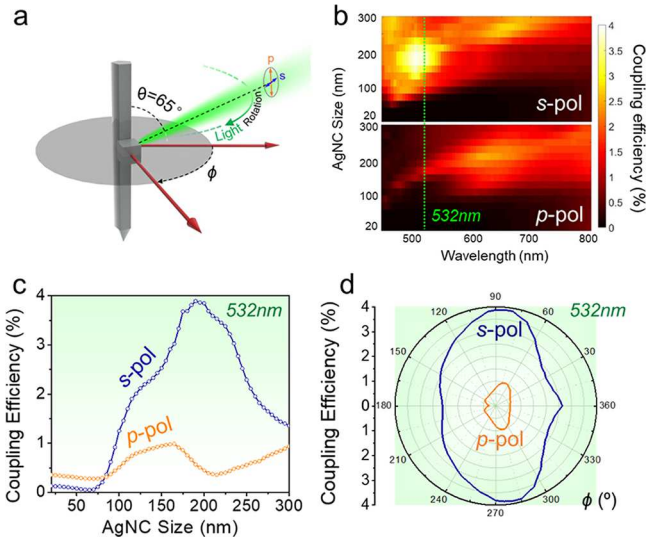

Figure 4. Optimization of the RE-TERS coupling efficiency. (a) Schematic diagram showing the parameters used to optimize in numerical simulations. The laser beam maintains a 65° incident angle with respect to the AgNW, as restricted by the equipment, while it can rotate around the AgNW (green arrow) and change the coupling angle (ϕ). The orientation of the *s*- and *p*-polarizations are marked by the navy blue and orange arrows. (b) Numerical simulations showing the coupling efficiency (%) as functions of incident light wavelength (450–800 nm) and AgNC size (20–300 nm) for both *s*- (top) and *p*- (bottom) polarizations. The green dashed line marks the laser wavelength (532 nm) used in the experiments with the profiles shown in (c). (d) Coupling efficiency dependence on the coupling angle (ϕ) for both polarizations.

the AgNW sidewall that is attached to the AgNC and the projection of the polarized Gaussian beam (beam waist = 1 μm) incidence direction. Because the AgNW has a pentagonal cross-section, its sidewalls are flat {100} facets and allow the AgNC to sit with one face in complete parallel with one of its sidewalls. As shown in Figure 4b, the *s*-polarization excitation (electric field perpendicular to the AgNW axis) generally gives higher coupling efficiency than the *p*-polarization, in particular near 532 nm wavelength, which benefits from the strong plasmonic enhancement of AgNWs in response to the *s*-polarization.[25,54] For 532 nm excitation (Figure 4c), the optimized AgNC size around 200 nm gives coupling efficiency near 4%, which is about 4 times higher than that of *p*-polarization. The azimuthal angle-dependence study in Figure 4d reveals that the coupling efficiency varies between 2–4% when the incident light is focused on the AgNW–AgNC junction from different directions (ϕ), providing a robust fabrication tolerance when attaching the bundle to the AFM cantilever.

The chemical sensitivity of a TERS probe in the direct-excitation configuration is typically characterized by the enhancement factor (EF), as given by the following equation

$$\mathrm{EF} = \left(\frac{I_{\mathrm{engaged}} - I_{\mathrm{retracted}}}{I_{\mathrm{retracted}}}\right)\frac{A_{\mathrm{background}}}{A_{\mathrm{TERS}}}$$

where I_{engaged} and $I_{\mathrm{retracted}}$ are Raman peak intensities measured with the tip in contact and retracted, $A_{\mathrm{background}}$ is the area of the excitation laser spot, and A_{TERS} is the effective area of the TERS enhancement region, giving that the molecular density is a constant during the measurement. The difference between I_{engaged} and $I_{\mathrm{retracted}}$ is the Raman signal generated due to the tip enhancement, or $I_{\mathrm{TERS}} = I_{\mathrm{engaged}} - I_{\mathrm{retracted}}$. It can be seen from this equation that molecules under the direct laser excitation will contribute to $I_{\mathrm{retracted}}$ but only those under the nanosized TERS spot, which depends on the tip radius and tip–substrate distance, will contribute to the TERS signal (I_{TERS}) that has nanoscale spatial resolution. Therefore, most of the molecules within the excitation laser spot become part of the background which limits both the TERS sensitivity and the spatial resolution. In remote excitation configuration, however, this diffraction-limited background is suppressed, because the laser focus is vertically separated from the scanning region, and the far-field radiation density reaching the detection spot is therefore reduced. This has been observed in other remote-excitation configurations, including grating couplers.[55] Apart from background suppression, the RE-TERS can also produce stronger signal compared to the conventional direct-excitation (DE) configuration under the same incident power. Although not yet experimentally demonstrated, the signal enhancement is theoretically possible when the power of optical excitation injected into the near-field region through the SPPs outweighs the antenna effect of the tip in DE-TERS with the apex capturing light over a cross-section exceeding its geometric dimensions. Nevertheless, this requires efficient optical coupling and low propagation loss of the RE-TERS configuration, which has been challenging to achieve.

In the comparative characterization of the RE- and DE-TERS shown in Figure 5, we demonstrated that the AgNC–AgNW-based RE-TERS probe can provide the benefit of both background suppression and signal enhancement, thus significantly improving the TERS contrast. Figure 5a,b illustrate the RE- and DE-TERS measurement configurations.

DOI: 10.1021/acs.nanolett.8b03399
Nano Lett. 2019, 19, 100–107

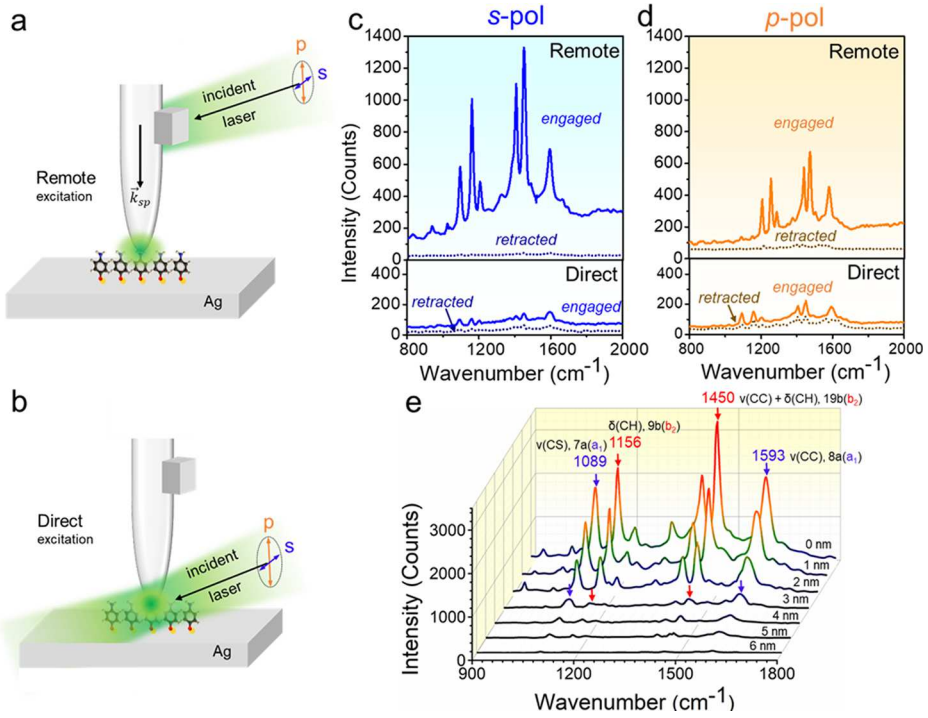

Figure 5. Comparison between RE-TERS with DE-TERS and dependence of RE-TERS signals on tip-to-substrate distance. (a,b) Schematics showing the remote (a) and direct (b) excitation methods. In both cases, *s*- and *p*-polarizations were examined on a self-assembled monolayer (SAM) of 4-ATP on an ultrasmooth Ag substrate. (c,d) 4-ATP Raman spectra measured with RE- and DE-TERS with incident lasers with *s*- (c) and *p*- (d) polarizations in both engaged (light color, solid lines) and retracted (dark color, dashed lines) modes. (e) As tip gets closer to the 4-ATP SAM sample, the overall signal increases drastically (*s*-polarization). At large tip−substrate distances, the peaks marked by blue arrows (1089 and 1593 cm^{-1}) have the highest intensities, consistent with regular SERS spectrum, whereas at smaller distances, the peaks marked by the red arrows (1156 and 1450 cm^{-1}) become dominating. Excitation: 532 nm, 0.2 mW at sample surface. Integration time = 2 s for (c,d) and 4 s for (e).

The same probe and laser power (6 mW) were used for all the measurements in Figure 5. In the RE-TERS experiment, the incident laser is focused on the AgNC, whereas in DE-TERS, the laser is focused directly on the AgNW tip. To ensure substrate and sample homogeneity, we used a self-assemble monolayer (SAM) of 4-aminothiophenol (4-ATP) on an ultrasmooth Ag thin film as the standard sample. The ultrasmooth Ag thin film was fabricated following the same protocol as the Au-thin film in Figure 2. With both *s*- and *p*-polarized incident light, the background ($I_{retracted}$) is significantly reduced in RE-TERS, with a background reduction ratio ($I_{retracted,RE}/I_{retracted,DE}$) of 0.26 and 0.52, respectively. Similarly, for both polarizations, the enhancements of the TERS signal in RE opposed to DE excitation were observed, featuring a signal enhancement ratio ($I_{engaged,RE}/I_{engaged,DE}$) of 12.2 (*s*-pol) and 3.3 (*p*-pol). Both calculations are based on the Gaussian fitting of the 1446 cm^{-1} peak. The signal enhancement from more efficient power injection than tip-scattering and the background reduction from the separation of the excitation and detection spots work synergistically to significantly increase the TERS contrast. Compared to the EF, the calculation of which is often based on many estimations, the TERS contrast, given by $C = \frac{I_{engaged}}{I_{retracted}}$,[56−58] is based purely on experimental data and is a direct measure of the signal increase by the tip and the image quality that can be obtained in a TERS experiment.[59] Therefore, *C* is of more practical relevance and has been adopted as the industrial standard for benchmarking the performance of TERS probe. Here, we have seen a $C_{RE\text{-}TERS}$ ∼ 100 for the *s*-polarization, which is enhanced from that of the same probe in the DE-TERS configuration by ∼47-fold. Even for the *p*-polarization that is not optimized for RE-TERS coupling, we still saw a 6-fold increase in TERS contrast with a $C_{RE\text{-}TERS}$ ∼ 20.

Figure 5e shows RE-TERS spectra as a function of tip−substrate distance (*d*) for 4-ATP SAM on ultrasmooth Ag thin film using an incident laser power of 6 mW at λ = 532 nm (0.2 mW at sample surface). The tip was first brought in contact with the substrate (defined as 0 nm), then the tip was gradually lifted by adjusting the set point in the feedback system of the contact mode AFM (Figure S5). The TERS signal dropped drastically when the gap distance increased beyond 2 nm and barely showed any Raman signature of 4-ATP at 6 nm, clearly demonstrating the near-field origin of the signal. We also note that although positions of the major Raman peaks stay constant at different gap distance, the relative peak intensity changed noticeably. At larger tip−substrate distances (>2 nm), the 1089 cm^{-1} peak corresponding to C−S stretching (ν(CS), 7a) and the 1593 cm^{-1} peak corresponding to C═C stretching (ν(CC), 8a) are the dominating peaks,[60] as marked by the blue arrows in Figure 5e. Both vibrations belong to a_1 symmetry of the 4-ATP, which has a C_{2v} symmetry point group. This is consistent with the surface selection rule, which dictates that for an adsorbed molecule with C_{2v} symmetry and its C_2 axis perpendicular to the metal surface, that the electromagnetic enhancement should obey the relationship of $a_1 > b_2$, $b_1 > a_2$.[60−62] However, for small tip−substrate distances (≤2 nm), the vibrations with b_2 symmetry at 1156 cm^{-1} (δ(CH), 9b) and the 1450 cm^{-1} (ν(CC) + δ(CH), 19b) quickly grow stronger than the a_1 peaks. Such strong anomaly has been previously observed in systems with tight optical confinement,

DOI: 10.1021/acs.nanolett.8b03399
Nano Lett. 2019, 19, 100−107

such as hollow plasmonic nanoparticles[63] or nanogaps[64,65] and can be attributed to the chemical enhancement effects, such as photoinduced charge transfer through the Herzberg–Teller contribution.[60,64,66,67] Figure 5e demonstrates the dependence of the "b_2 enhancement" on the gap size or the degree of confinement.

Conclusions. In summary, using AgNCs with proper size as an efficient plasmonic antenna to convert the excitation laser beam into the surface plasmon polaritons on a sharp-tip AgNW waveguide, we have demonstrated the remote-excitation of tip-enhanced Raman spectroscopy with high TERS contrast (up to 100) and fine spatial resolution (10 nm). We mapped the Raman scattering variation within a MoS_2 flake, which reveals the strain distribution stored during the transfer process. The RE-TERS probes can be fabricated through a facile, robust and reproducible method, which requires only economical benchtop techniques. This polarization-insensitive antenna design allows the choosing of laser polarization that has weak interaction with the sample substrate for the further reduction of background noise. We expect that the remote-excitation plasmonic probe offers new routes for applications in disciplines where high resolution and sensitivities are needed, for example, in near-field scanning optical imaging and sensing.

Methods. *AgNC–AgNW Bundle Synthesis and Probe Preparation.* The AgNW solution (concentration ~10^8/mL, solved in ethanol) and AgNC solution (concentration ~10^{11}/mL, solved in ethanol) were mixed and then incubated for 48 h at room temperature to form AgNC–AgNW bundles. After incubation, the top clean solution was removed and the bottom solution containing bundles was casted on a PDMS substrate and dried with nitrogen. The averaged AgNC density on an AgNW can be controlled by varying the volume ratio of AgNW and AgNC solutions, as shown in Figure S2. The final AgNC density of ~0.7 μm^{-1} (on AgNW) was used in this experiment, which gave the highest chance to find a single AgNC around 2–6 μm away from the AgNW tip. The bundle samples on PDMS substrate were then examined under a dark-field optical microscope (Nikon Eclipse Ni–U, 50× objective lens)[68,69] and a sCMOS camera (Zyla 5.5, Andor). With proper contrast settings in the camera, the AgNCs can be identified from the AgNW. A sharp tungsten probe controlled by a high-precision motorized micromanipulator (Sutter Instrument Co.) was then used to gently wipe along the selected AgNW to remove the unnecessary AgNCs from the AgNW, then pick it up and mount onto the side wall of a conventional silicon AFM cantilever (Olympus, Model AC160TS-R3). The prepared probe was usually used within 3 days of fabrication to avoid oxidization.

TERS Measurement. The TERS measurement illustrated in Figure 1a was carried out on an OmegaScope 1000 (AIST-NT) platform, which is integrated with a Horiba confocal Raman microscope (LabRAM HR Evolution). The 532 nm laser beam (OPUS 532, Laser Quantum) was sent through two tandem laser line filters, a quarter-λ wave plate, and a linear polarizer to generate a *s*-polarized beam. A high NA objective lens (Mitutoyo, M Plan Apo 100×, NA = 0.7) was used to focus the off-axis excitation beam onto the AgNC–AgNW junction and collect the Raman scattering from the AgNW sharp tip. The contact-mode AFM was used to perform the TERS measurement in ambient conditions.

Numerical Simulation. Electromagnetic simulations were carried out using a commercial finite element analysis software (COMSOL Multiphysics 5.1). The AgNW diameter was 200 nm and the AgNC size was swept from 20 to 300 nm. The tip radius of the AgNW was 5 nm and the gap between AgNC and AgNW was set at 2 nm, to include the influence from polyvinylpyrrolidone (PVP) molecules. The distance from the AgNW–AgNC junction to the AgNW tip was 2 μm. The silver permittivity was obtained from fitting the Drude model from Johnson and Christy.[70]

■ ASSOCIATED CONTENT

Supporting Information

The Supporting Information is available free of charge on the ACS Publications website at DOI: 10.1021/acs.nanolett.8b03399.

Additional information on coupling efficiency measurement, AgNC density control, AgNC removal, MoS_2 TERS imaging resolution, control of tip-to-substrate distance, numerical simulations, AgNW probe quality control, sample preparation (PDF)

Video showing removal of large AgNCs (AVI)

■ AUTHOR INFORMATION

Corresponding Author

*E-mail: ming@ece.ucr.edu.

ORCID

Xuezhi Ma: 0000-0003-3607-1145
Yangzhi Zhu: 0000-0003-2920-3365
Qiushi Liu: 0000-0002-9017-2492
Da Xu: 0000-0002-7554-426X
Ming Liu: 0000-0001-9849-1845

Notes

The authors declare no competing financial interest.

■ ACKNOWLEDGMENTS

This work is supported by NSF Grants CAREER DMR-1654746 and CHE-1654794.

■ REFERENCES

(1) Stockle, R. M.; Suh, Y. D.; Deckert, V.; Zenobi, R. *Chem. Phys. Lett.* **2000**, *318* (1–3), 131–136.
(2) Hayazawa, N.; Inouye, Y.; Sekkat, Z.; Kawata, S. *Opt. Commun.* **2000**, *183* (1–4), 333–336.
(3) Anderson, M. S. *Appl. Phys. Lett.* **2000**, *76* (21), 3130–3132.
(4) Pettinger, B.; Picardi, G.; Schuster, R.; Ertl, G. *Electrochemistry* **2000**, *68* (12), 942–949.
(5) Zrimsek, A. B.; Chiang, N.; Mattei, M.; Zaleski, S.; McAnally, M. O.; Chapman, C. T.; Henry, A.-I.; Schatz, G. C.; Van Duyne, R. P. *Chem. Rev.* **2017**, *117* (11), 7583–7613.
(6) Richard-Lacroix, M.; Zhang, Y.; Dong, Z.; Deckert, V. *Chem. Soc. Rev.* **2017**, *46* (13), 3922–3944.
(7) Li, Z. Y. *Adv. Opt. Mater.* **2018**, *6* (16), 1701097.
(8) Chiang, N.; Chen, X.; Goubert, G.; Chulhai, D. V.; Chen, X.; Pozzi, E. A.; Jiang, N.; Hersam, M. C.; Seideman, T.; Jensen, L.; et al. *Nano Lett.* **2016**, *16* (12), 7774–7778.
(9) Zhang, R.; Zhang, Y.; Dong, Z. C.; Jiang, S.; Zhang, C.; Chen, L. G.; Zhang, L.; Liao, Y.; Aizpurua, J.; Luo, Y.; Yang, J. L.; Hou, J. G. *Nature* **2013**, *498* (7452), 82–86.
(10) Ropers, C.; Neacsu, C. C.; Elsaesser, T.; Albrecht, M.; Raschke, M. B.; Lienau, C. *Nano Lett.* **2007**, *7* (9), 2784–2788.
(11) De Angelis, F.; Das, G.; Candeloro, P.; Patrini, M.; Galli, M.; Bek, A.; Lazzarino, M.; Maksymov, I.; Liberale, C.; Andreani, L. C.; Di Fabrizio, E. *Nat. Nanotechnol.* **2010**, *5* (1), 67–72.

DOI: 10.1021/acs.nanolett.8b03399
Nano Lett. 2019, 19, 100–107

(12) Berweger, S.; Atkin, J. M.; Olmon, R. L.; Raschke, M. B. *J. Phys. Chem. Lett.* **2010**, *1* (24), 3427−3432.
(13) Yu, J.; Saito, Y.; Ichimura, T.; Kawata, S.; Verma, P. *Appl. Phys. Lett.* **2013**, *102* (12), 123110.
(14) Wang, Y.; Srituravanich, W.; Sun, C.; Zhang, X. *Nano Lett.* **2008**, *8* (9), 3041−3045.
(15) Kravtsov, V.; Ulbricht, R.; Atkin, J.; Raschke, M. B. *Nat. Nanotechnol.* **2016**, *11* (5), 459.
(16) Schambach, P. *Tip-enhanced Raman spectroscopy in ultra-high vacuum* **2013**.
(17) Fujita, Y.; et al. *Jpn. J. Appl. Phys.* **2016**, *55* (8S1), 08NA02.
(18) Russell, K. J.; Liu, T.-L.; Cui, S.; Hu, E. L. *Nat. Photonics* **2012**, *6*, 459.
(19) Tao, A.; Kim, F.; Hess, C.; Goldberger, J.; He, R.; Sun, Y.; Xia, Y.; Yang, P. *Nano Lett.* **2003**, *3* (9), 1229−1233.
(20) Ma, X. Z.; Zhu, Y. Z.; Kim, S.; Liu, Q. S.; Byrley, P.; Wei, Y.; Zhang, J.; Jiang, K. L.; Fan, S. S.; Yan, R. X.; Liu, M. *Nano Lett.* **2016**, *16* (11), 6896−6902.
(21) Kim, S.; Bailey, S.; Liu, M.; Yan, R. X. *Nano Res.* **2017**, *10* (7), 2395−2404.
(22) Ditlbacher, H.; Hohenau, A.; Wagner, D.; Kreibig, U.; Rogers, M.; Hofer, F.; Aussenegg, F. R.; Krenn, J. R. *Phys. Rev. Lett.* **2005**, *95* (25), 257403.
(23) Yan, R.; Pausauskie, P.; Huang, J.; Yang, P. *Proc. Natl. Acad. Sci. U. S. A.* **2009**, *106* (50), 21045−21050.
(24) Wang, W.; Yang, Q.; Fan, F.; Xu, H.; Wang, Z. L. *Nano Lett.* **2011**, *11* (4), 1603−1608.
(25) Knight, M. W.; Grady, N. K.; Bardhan, R.; Hao, F.; Nordlander, P.; Halas, N. J. *Nano Lett.* **2007**, *7* (8), 2346−2350.
(26) Sanders, A. W.; Routenberg, D. A.; Wiley, B. J.; Xia, Y.; Dufresne, E. R.; Reed, M. A. *Nano Lett.* **2006**, *6* (8), 1822−1826.
(27) Tao, A.; Sinsermsuksakul, P.; Yang, P. *Nat. Nanotechnol.* **2007**, *2*, 435.
(28) Tao, A. R.; Huang, J.; Yang, P. *Acc. Chem. Res.* **2008**, *41* (12), 1662−1673.
(29) Liu, Z.; Amani, M.; Najmaei, S.; Xu, Q.; Zou, X. L.; Zhou, W.; Yu, T.; Qiu, C. Y.; Birdwell, A. G.; Crowne, F. J.; Vajtai, R.; Yakobson, B. I.; Xia, Z. H.; Dubey, M.; Ajayan, P. M.; Lou, J. *Nat. Commun.* **2014**, *5*, 5246.
(30) Kazemi-Zanjani, N.; Kergrene, E.; Liu, L.; Sham, T.-K.; Lagugné-Labarthet, F. *Sensors* **2013**, *13* (10), 12744.
(31) Hermann, P.; Hecker, M.; Chumakov, D.; Weisheit, M.; Rinderknecht, J.; Shelaev, A.; Dorozhkin, P.; Eng, L. M. *Ultramicroscopy* **2011**, *111* (11), 1630−1635.
(32) Tarun, A.; Hayazawa, N.; Motohashi, M.; Kawata, S. *Rev. Sci. Instrum.* **2008**, *79* (1), 013706.
(33) Hayazawa, N.; et al. *J. Raman Spectrosc.* **2007**, *38* (6), 684−696.
(34) Saito, Y.; Motohashi, M.; Hayazawa, N.; Iyoki, M.; Kawata, S. *Appl. Phys. Lett.* **2006**, *88* (14), 143109.
(35) Pozzi, E. A.; Goubert, G.; Chiang, N.; Jiang, N.; Chapman, C. T.; McAnally, M. O.; Henry, A.-I.; Seideman, T.; Schatz, G. C.; Hersam, M. C.; Duyne, R. P. V. *Chem. Rev.* **2017**, *117* (7), 4961−4982.
(36) Lloyd, D.; Liu, X.; Christopher, J. W.; Cantley, L.; Wadehra, A.; Kim, B. L.; Goldberg, B. B.; Swan, A. K.; Bunch, J. S. *Nano Lett.* **2016**, *16* (9), 5836−5841.
(37) He, K.; Poole, C.; Mak, K. F.; Shan, J. *Nano Lett.* **2013**, *13* (6), 2931−2936.
(38) Jariwala, D.; Sangwan, V. K.; Lauhon, L. J.; Marks, T. J.; Hersam, M. C. *ACS Nano* **2014**, *8* (2), 1102−1120.
(39) Rahaman, M.; Rodriguez, R. D.; Plechinger, G.; Moras, S.; Schüller, C.; Korn, T.; Zahn, D. R. T. *Nano Lett.* **2017**, *17* (10), 6027−6033.
(40) Milekhin, A. G.; Rahaman, M.; Rodyakina, E. E.; Latyshev, A. V.; Dzhagan, V. M.; Zahn, D. R. T. *Nanoscale* **2018**, *10* (6), 2755−2763.
(41) van der Zande, A. M.; Huang, P. Y.; Chenet, D. A.; Berkelbach, T. C.; You, Y.; Lee, G.-H.; Heinz, T. F.; Reichman, D. R.; Muller, D. A.; Hone, J. C. *Nat. Mater.* **2013**, *12*, 554.
(42) Nagpal, P.; Lindquist, N. C.; Oh, S.-H.; Norris, D. J. *Science* **2009**, *325* (5940), 594.
(43) Ma, X.; Liu, Q.; Xu, D.; Zhu, Y.; Kim, S.; Cui, Y.; Zhong, L.; Liu, M. *Nano Lett.* **2017**, *17* (11), 6961−6967.
(44) Wakabayashi, N.; Smith, H. G.; Nicklow, R. M. *Phys. Rev. B* **1975**, *12* (2), 659−663.
(45) Zhang, W.; Cui; Yeo, B.-S.; Schmid, T.; Hafner, C.; Zenobi, R. *Nano Lett.* **2007**, *7* (5), 1401−1405.
(46) Lee, C.; Yan, H.; Brus, L. E.; Heinz, T. F.; Hone, J.; Ryu, S. *ACS Nano* **2010**, *4* (5), 2695−2700.
(47) Chen, S.-Y.; Zheng, C.; Fuhrer, M. S.; Yan, J. *Nano Lett.* **2015**, *15* (4), 2526−2532.
(48) Carvalho, B. R.; Malard, L. M.; Alves, J. M.; Fantini, C.; Pimenta, M. A. *Phys. Rev. Lett.* **2015**, *114* (13), 136403.
(49) Rahaman, M.; Rodriguez, R. D.; Plechinger, G.; Moras, S.; Schüller, C.; Korn, T.; Zahn, D. R. *Nano Lett.* **2017**, *17* (10), 6027−6033.
(50) Conley, H. J.; Wang, B.; Ziegler, J. I.; Haglund, R. F.; Pantelides, S. T.; Bolotin, K. I. *Nano Lett.* **2013**, *13* (8), 3626−3630.
(51) Zhou, K. G.; Withers, F.; Cao, Y.; Hu, S.; Yu, G. L.; Casiraghi, C. *ACS Nano* **2014**, *8* (10), 9914−9924.
(52) Li, H.; Zhang, Q.; Yap, C. C. R.; Tay, B. K.; Edwin, T. H. T.; Olivier, A.; Baillargeat, D. *Adv. Funct. Mater.* **2012**, *22* (7), 1385−1390.
(53) Wei, H.; Hao, F.; Huang, Y. Z.; Wang, W. Z.; Nordlander, P.; Xu, H. X. *Nano Lett.* **2008**, *8* (8), 2497−2502.
(54) Fang, Y. R.; Wei, H.; Hao, F.; Nordlander, P.; Xu, H. X. *Nano Lett.* **2009**, *9* (5), 2049−2053.
(55) Berweger, S.; Atkin, J. M.; Olmon, R. L.; Raschke, M. B. *J. Phys. Chem. Lett.* **2010**, *1* (24), 3427−3432.
(56) Stöckle, R. M.; Suh, Y. D.; Deckert, V.; Zenobi, R. *Chem. Phys. Lett.* **2000**, *318* (1), 131−136.
(57) Pettinger, B.; Ren, B.; Picardi, G.; Schuster, R.; Ertl, G. *Phys. Rev. Lett.* **2004**, *92* (9), 096101.
(58) Meyer, C.; et al. *J. Raman Spectrosc.* **2017**, *48* (1), 46−52.
(59) Stadler, J.; Schmid, T.; Zenobi, R. *Nanoscale* **2012**, *4* (6), 1856−1870.
(60) Osawa, M.; Matsuda, N.; Yoshii, K.; Uchida, I. *J. Phys. Chem.* **1994**, *98* (48), 12702−12707.
(61) Creighton, J. A. *Surf. Sci.* **1986**, *173* (2), 665−672.
(62) Zheng, J.; Zhou, Y.; Li, X.; Ji, Y.; Lu, T.; Gu, R. *Langmuir* **2003**, *19* (3), 632−636.
(63) Wang, Y.; Chen, H.; Dong, S.; Wang, E. *J. Chem. Phys.* **2006**, *125* (4), 044710.
(64) Zhou, Q.; et al. *Angew. Chem., Int. Ed.* **2006**, *45* (24), 3970−3973.
(65) Fromm, D. P.; Sundaramurthy, A.; Kinkhabwala, A.; Schuck, P. J.; Kino, G. S.; Moerner, W. E. *J. Chem. Phys.* **2006**, *124* (6), 061101.
(66) Chenal, C.; et al. *ChemPhysChem* **2008**, *9* (11), 1617−1623.
(67) Matsuda, N.; et al. *Chem. Lett.* **1992**, *21* (7), 1385−1388.
(68) Itoh, T.; Yamamoto, Y. S.; Kitahama, Y.; Balachandran, J. *Phys. Rev. B: Condens. Matter Mater. Phys.* **2017**, *95* (11), 115441.
(69) Itoh, T.; Yamamoto, Y. S.; Suzuki, T.; Kitahama, Y.; Ozaki, Y. *Appl. Phys. Lett.* **2016**, *108* (2), 021604.
(70) Johnson, P. B.; Christy, R.-W. *Phys. Rev. B* **1972**, *6* (12), 4370.

DOI: 10.1021/acs.nanolett.8b03399
Nano Lett. 2019, 19, 100−107